Mechanism and Machine Theory 167 (2022) 104555

Contents lists available at ScienceDirect

Mechanism and Machine Theory

journal homepage: www.elsevier.com/locate/mechmt

A compliant guiding mechanism utilizing orthogonally oriented flexures with enhanced stiffness in degrees-of-constraint

Ruiqi Li [a], Zhijun Yang [a,c,*], Bingyu Cai [a], Guimin Chen [b], Baisheng Wu [a], Yutai Wei [a]

[a] State Key Laboratory for Precision Electronics Manufacturing Technology and Equipment, Guangdong University of Technology, Guangzhou 510006, China
[b] State Key Laboratory for Manufacturing Systems Engineering and Shanxi Key Lab of Intelligent Robots, Xi'an Jiaotong University, Xi'an 710049, China
[c] Foshan Huadao Ultra Precision Tech. LTD. , Foshan 528225, China

ARTICLE INFO

Keywords:
Nonlinear deflection
Stress constraint
Large stroke
Orthogonally oriented flexures
Energy method

ABSTRACT

The large stroke is usually realized by lowering stiffness along the degrees of freedom, which usually leads to a decrease of stiffness along the degrees of constraint. A high stiffness ratio is crucial for reducing the deflections induced by disturbances such as eccentric force and the gravity of the load. Besides, the fatigue life of these mechanisms will be shortened due to the large stress caused by the large deflection. This paper proposed a new guiding mechanism using orthogonally oriented flexures to improve the stiffness along the degrees of constraint and reduce stress concentration. The energy method is utilized to obtain the kinetostatic model of the guiding mechanism by taking the nonlinear deflection into account, based on which the mechanism is optimized by simultaneously considering the topology and size. As compared to the performance of traditional design obtained through the same optimization objective and constraints, the optimal design effectively improves the stiffness along the degrees of constraint, whose accuracy is also validated by the finite element analysis results. Experimental results show that the proposed mechanism increases the stiffness ratio $K_{\alpha z}/K_x$ by 3.54 times compared to the traditional mechanism.

1. Introduction

Compliant mechanisms, capable of providing nanometer resolution by eliminating wear, friction and backlash, have been widely used in various precision devices for precision positioning [1–7], micro-manipulation [8–10], microgripper [11], and microscopy [12–14], which are commonly driven by linear actuators such as piezoelectric actuators (PZT) [15–17] and voice coil motors (VCM) [5,13,18,19]. A PZT actuator exhibits high-speed responses for its high stiffness and can provide large driving forces, while the stroke is limited to 0.1% of its length. Therefore, an amplifying compliant mechanism is usually employed to extend the travel range of the PZT actuator, and a guiding compliant mechanism is designed to minimize the parasitic motions of the amplifying mechanism along its degrees of constraint (DOC) [17,20–23].

A VCM provides a larger actuation stroke, but the travel range is limited by the actuation force required by the compliant mechanism. Thus, leaf springs are often chosen for the design of linear guiding mechanisms to reduce the stiffness along the guiding

* Corresponding author.
E-mail address: yangzj@gdut.edu.cn (Z. Yang).

https://doi.org/10.1016/j.mechmachtheory.2021.104555
Received 12 May 2021; Received in revised form 6 September 2021; Accepted 7 September 2021
Available online 23 September 2021

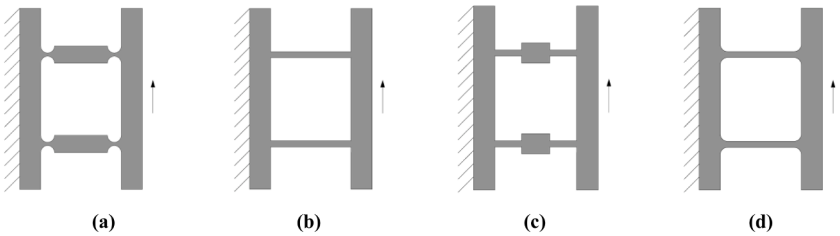

Fig. 1. Guiding mechanism with the same topology (a) NFHs type, (b) leaf-springs type, (c) leaf-springs type with intermediate semi-rigid elements, and (d) CFLSs type.

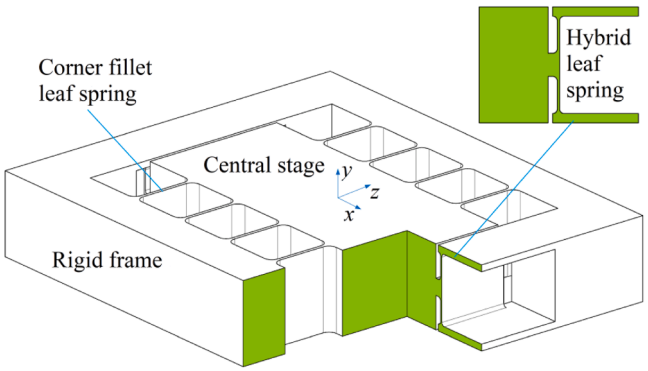

Fig. 2. Cutaway view of the guiding mechanism designed with CFLSs and HLSs.

direction [24–29]. Compliant compound parallelogram mechanisms (CCPM) are the typical guiding mechanisms designed with leaf springs. Hao and Kong used CCPM to design a large-range XY compliant parallel manipulator in Ref. [29], whose motion range reaches 20 × 20 mm. Ref. [25] extended the travel range of a linear-motion mechanism by utilizing the compressed-soft effect of leaf spring to reduce the stiffness along its degrees of freedom (DOF). However, low stiffness along the DOC is also prone to occur in these mechanisms for the large ratio of length to thickness of leaf springs (l/t), which leads to an increase of deflection caused by the disturbing loads. Therefore, the present CCPMs have limited efficiency in some applications with additional loads along the DOCs. To enhance the out-of-plane stiffness of CCPMs, Ref. [29] increased the beam number and utilized spatial compliant legs. Although the out-of-plane stiffness is improved in this way, the driving stiffness is also increased. For the compliant mechanism subjected to torsional moment due to the deviation of driving force from the motion center [30], improving the ratio of stiffness along the DOCs to it along the DOF is a more efficient method to decrease the disturbance displacement.

On the other hand, the maximum stress of compliant elements has a crucial influence on the fatigue life of compliant mechanisms, which have been well researched for the notch flexure hinges in Ref. [31]. The sudden shape change of leaf springs generates notable stress concentration characteristics which enlarged the maximum stress of mechanisms greatly. Therefore, Ref. [32] investigates the scope for stress reduction through shape optimization of the leaf springs, in which the maximum stress is calculated under the small deflection assumption. In fact, the load-deflection relationship of CCPMs presents obvious nonlinearities for the initial internal axial force [26]. The nonlinearity and stress concentration characteristics of leaf springs without corner curves make it difficult to evaluate the maximum stress at the first stage of mechanism design. In order to model the stress of leaf springs in large-stroke applications, a nonlinear model of corner-fillet leaf springs (CFLS) is provided in Ref. [33] in which the induced fillet improved the maximum stress effectively.

Considering the limitations of current design methods for guiding mechanisms, this article proposed a new guiding mechanism utilizing orthogonally oriented CFLSs and hybrid leaf springs (HLSs). Although it is a usual way to neglect the effect of small fillets during design, tiny fillets have limited improvement in the reduction of maximum stress. Thus nonlinear models of CFLSs and HLSs are adopted in this work for the accurate stress design. The nonlinear energy formula of the guiding mechanism is provided to obtain the kinetostatic model by taking the nonlinear deflection of CFLSs and HLSs into account, and the corresponding nonlinear stress is calculated using the nonlinear model. The simultaneous optimal design of topology and size is carried out to minimize the maximum stress and mass of the mechanism by determining the optimal group number and parameters of CFLSs and HLSs.

The main contents of the paper are arranged as follows: Section 2 introduces the design of the new guiding mechanism in detail. The kinetostatic model of the guiding mechanism is established and the nonlinear stress is calculated in Section 3. The optimized design is illustrated in Section 4 and a design case is provided to explain its efficiency. The performance of the optimal design is verified using the finite element analysis (FEA) method in Section 5. Comparison is accomplished in Section 6 to demonstrate the improvement of the proposed mechanism. Experimental results are obtained in Section 7. Conclusions are drawn in the last section of this paper.

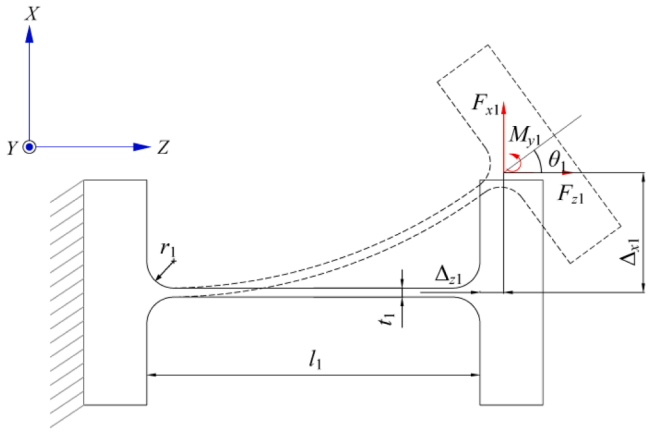

Fig. 3. Nonlinear deflection of the fixed-free CFLS.

2. Design

Fig. 1 shows several compliant guiding mechanism designs of parallelogram structures. The guiding mechanism utilizing notch flexure hinges (NFHs), as shown in Fig. 1(a), provides high stiffness and high frequency, but the travel range of these mechanisms is limited to several micrometers due to the low deflection capability of NFHs. Leaf-springs provide good compliance for the guiding mechanisms as shown in Fig. 1(b), but the stiffness along the DOC of these guiding mechanisms is smaller than that of the NFHs-based guiding mechanisms. Although increasing the width of leaf springs can enhance the stiffness along the DOC and avoid high driving stiffness, it's adverse for the compact design. Leaf-springs with intermediate semi-rigid elements [24,34] were suggested to improve the stiffness of leaf springs along the DOC, as shown in Fig. 1(c), but this would increase the stiffness along the DOF and intensify the stress concentration due to the sudden cross-section change. Although CFLSs were developed to reduce the stress concentration of the guiding mechanism, as shown in Fig. 1(d), the improvement with the stiffness along the DOC is restricted by the compact structure.

To improve the stiffness along the DOC and lower the stress concentration of the leaf-spring-based mechanism, a new guiding mechanism utilizing orthogonally oriented CFLSs and HLSs is designed, as depicted in Fig. 2. CFLSs are horizontally placed in a symmetric configuration to eliminate the parasitic motions and provide a relatively large motion between the rigid frame and central stage. Two pairs of HLSs are arranged vertically on both ends of the central stage along the DOF direction to strengthen the payload stiffness and avoid pitch motion.

3. Analytical modeling of the guiding mechanism

The driving force applied on the guiding mechanism causes remarkable tension stress in the deflected CFLSs and HLSs, leading to stress stiffening of the mechanism along the DOF. Therefore, the load-displacement relationship of the guiding mechanism presents a non-negligible nonlinearity.

3.1. Deflection of CFLS

As shown in Fig. 3, the radius of fillets, the minimum thickness, the length, and the width of a CFLS are denoted as r_1, t_1, l_1, and w_1, respectively.

The loads applied on CFLS and the corresponding deflections are normalized as:

$$m_1 = \frac{M_{y1} l_1}{E_1 I_1}, f_1 = \frac{F_{x1} l_1^2}{E_1 I_1}, p_1 = \frac{F_{z1} l_1^2}{E_1 I_1}, u_{x1} = \frac{\Delta_{x1}}{l_1}, u_{z1} = \frac{\Delta_{z1}}{l_1} \tag{1}$$

where I_1 is the second moment of area about the Y-axis of CFLS, and E_1 is the Young's modulus of the material.

By taking $\eta_1 = r_1/l_1$, the nonlinear deflection of a fixed-free CFLS can be calculated using the following equations [33]:

$$\begin{bmatrix} f_1 \\ m_1 \end{bmatrix} = \begin{bmatrix} k'^0_{11} & k'^0_{12} \\ k'^0_{12} & k'^0_{13} \end{bmatrix} \begin{bmatrix} u_{x1} \\ \theta_1 \end{bmatrix} + p_1 \begin{bmatrix} \dfrac{1.2}{\lambda_1} & -0.1 \\ -0.1 & \dfrac{2\lambda_1}{15} \end{bmatrix} \begin{bmatrix} u_{x1} \\ \theta_1 \end{bmatrix} \tag{2}$$

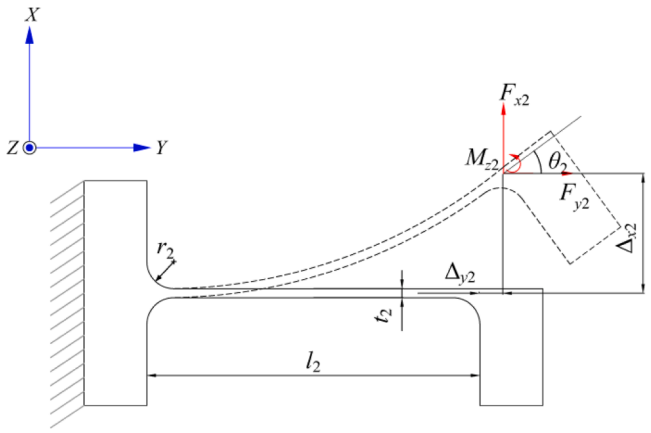

Fig. 4. Nonlinear deflection of the fixed-free HLS.

$$u_{z1} = \frac{p_1\lambda_1}{12b_1^2} - \frac{1}{2}\begin{bmatrix} u_{x1} & \theta_1 \end{bmatrix}\begin{bmatrix} \frac{1.2}{\lambda_1} & -0.1 \\ -0.1 & \frac{2\lambda_1}{15} \end{bmatrix}\begin{bmatrix} u_{x1} \\ \theta_1 \end{bmatrix} \tag{3}$$

where $k'^{0}_{11} = \frac{2g_{11}(a_1)\eta_1+1}{H_1}$, $k'^{0}_{12} = -\frac{1+2g_{11}(a_1)\eta_1}{2H_1}$, $k'^{0}_{13} = \frac{1+3g_{11}(a_1)\eta_1+3g_{12}(a_1)\eta_1^2+6g_{13}(a_1)\eta_1^3}{3H_1}$,

$H_1 = \left(\frac{1}{3} + g_{11}(a_1)\eta_1 + g_{12}(a_1)\eta_1^2 + 2g_{13}(a_1)\eta_1^3\right)\left(2g_{11}(a_1)\eta_1 + 1\right) - \left(\frac{1}{2} + g_{11}(a_1)\eta_1\right)^2$, $k'^{0}_{14} = \frac{12b_1^2}{\lambda_1}$, $\lambda_1 = (1 + 2g_{14}(a_1)\eta_1)$, and expressions of g_{1i} $(i = 1, 2, 3, 4)$ are listed in Appendix A.

The bending deflection of a fixed-guided CFLS in the *Y*-axis direction is in a small range which can be obtained using Castigliano's second theorem. For the situation that the width is large than 1/5 of the length, the shearing effect has a remarkable influence on the deflection. We have:

$$\Delta_{y1} = \frac{3t_1^2F_y}{E_1w_1^3}\int_0^{b_1}\frac{(b_1-2z)^2}{\zeta(z)}dz + \frac{6F_y}{5Gw_1}\int_0^{b_1}\frac{1}{\zeta(z)}dz \tag{4}$$

where $G = E_1/(2(1+\mu))$ is the shear modulus and μ is the Poisson's ratio. Then the bending stiffness in the *Y*-axis direction is yielded:

$$K_{y1} = E_1w_1^3/\left(3t_1^2A_1(a_1,b_1) + 2.4(1+\mu)w_1^2\lambda_1b_1\right) \tag{5}$$

where the expression of A_1 is shown in Appendix A.

The torsional stiffness for a CFLS around the *Z*-axis can be calculated using the following equation:

$$K_{az1} = f(\delta_1)\Bigg/\left(\int_0^{l_1}\frac{7}{2Gw_1t(x)^3}dx + \int_0^{l_1}\frac{7}{2Gw_1^3t(x)}dx\right)(\delta_1 = t_1/w_1) \tag{6}$$

where $f(\delta)$ is defined as Eq. (7) according to Ref. [35].

$$f(\delta) = \frac{1.17\delta^2 + 2.19\delta + 1.17}{\delta^2 + 2.61\delta + 1} \tag{7}$$

3.2. Deflection of HLS

The radius of fillets, the minimum thickness, the length, and the width of HLS are defined as r_2, t_2, l_2, and w_2, respectively, as shown in Fig. 4. The thickness function of HLS along the axial direction is expressed as ($a_2 = r_2/t_2$, $b_2 = l_2/t_2$):

$$\zeta(y) = \begin{cases} 2\left(a_2 - \sqrt{{a_2}^2 - (a_2-y)^2}\right) + 1, & 0 < y < a_2 \\ 1, & a_2 < y < b_2 - a_2 \\ \left(a_2 - \sqrt{{a_2}^2 - (y-b_2+a_2)^2}\right) + 1, & b_2 - a_2 < y < b_2 \end{cases} \tag{8}$$

The loads applied on HLS and the corresponding deflections are normalized:

$$m_2 = \frac{M_{z2} l_2}{E_2 I_2}, f_2 = \frac{F_{x2} l_2^2}{E_2 I_2}, p_2 = \frac{F_{y2} l_2^2}{E_2 I_2}, u_{x2} = \frac{\Delta_{x2}}{l_2}, u_{y2} = \frac{\Delta_{y2}}{l_2} \tag{9}$$

where I_2 is the second moment of area about the Z-axis of HLS and E_2 is the Young's modulus of the material.

A number of methods have been developed for the nonlinear deflection of leaf spring, such as elliptic integral solutions, beam constraint model, and pseudo-rigid-body models (PRBM). But these methods can't be used to predict the nonlinear deflection of flexure hinge with variable cross-section. Ref. [33] provides a nonlinear model for CFLS (NCFLS) to improve the stress concentration of leaf spring by considering the influence of corner-fillet on the nonlinear deflection. According to the NCFLS, the nonlinear stiffness of the flexure hinge is consists of the elastic stiffness and the stiffening/compressed stiffness caused by the axial load. Thus, the load-deflection relationship of HLS can be expressed as:

$$\begin{bmatrix} f_2 \\ m_2 \end{bmatrix} = \begin{bmatrix} k'^0_{21} & k'^0_{22} \\ k'^0_{22} & k'^0_{23} \end{bmatrix} \begin{bmatrix} u_{x2} \\ \theta_2 \end{bmatrix} + p_2 \begin{bmatrix} k'^1_{21} & k'^1_{22} \\ k'^1_{22} & k'^1_{23} \end{bmatrix} \begin{bmatrix} u_{x2} \\ \theta_2 \end{bmatrix} \tag{10}$$

$$u_{y2} = \frac{p}{k'^0_{24}} - \frac{1}{2} \begin{bmatrix} u_{x2} & \theta_2 \end{bmatrix} \begin{bmatrix} k'^1_{21} & k'^1_{22} \\ k'^1_{22} & k'^1_{23} \end{bmatrix} \begin{bmatrix} u_{x2} \\ \theta_2 \end{bmatrix} \tag{11}$$

where k'^0_{2i} $(i = 1,2,3,4)$ is the elastic stiffness coefficients of HLS, which is calculated by using Castigliano's theorem.

The load-stiffening coefficients can be expressed as:

$$k'^1_{21} = \frac{1.2}{\lambda_2}, k'^1_{22} = -0.1, k'^1_{23} = \frac{2\lambda_2}{15} \tag{12}$$

where λ_2 is the length-decrease coefficient of HLS and can be calculated using the following integral:

$$\lambda_2 = \frac{1}{b_2} \int_0^{b_2} \frac{1}{\zeta(y)} dy \tag{13}$$

By taking $\eta_2 = r_2/l_2$, the nonlinear deflection of HLS can be expressed as the following equations:

$$\begin{bmatrix} f_2 \\ m_2 \end{bmatrix} = \begin{bmatrix} \dfrac{(g_{11}(a_2) + g_{21}(a_2))\eta_2 + 1}{H_2} & -\dfrac{1 + 2g_{11}(a_2)\eta_2 + (g_{12}(a_2) + g_{22}(a_2))}{2H_2} \\ -\dfrac{1 + 2g_{11}(a_2)\eta_2 + (g_{12}(a_2) + g_{22}(a_2))}{2H_2} & \dfrac{1 + 3g_{11}(a_2)\eta_2 + 3g_{12}(a_2)\eta_2^2 + 3(g_{13}(a_2) + g_{23}(a_2))\eta_2^3}{3H_2} \end{bmatrix} \begin{bmatrix} u_{x2} \\ \theta_2 \end{bmatrix} + p_2 \begin{bmatrix} \dfrac{1.2}{1 + (g_{14}(a_2) + g_{24}(a_2))\eta_2} & -0.1 \\ -0.1 & \dfrac{2((g_{14}(a_2) + g_{24}(a_2))\eta_2)}{15} \end{bmatrix} \begin{bmatrix} u_{x2} \\ \theta_2 \end{bmatrix} \tag{14}$$

$$u_{y2} = \frac{p_2(1 + (g_{14}(a_2) + g_{24}(a_2))\eta_2)}{12b_2^2} - \frac{1}{2} \begin{bmatrix} u_{x2} & \theta_2 \end{bmatrix} \begin{bmatrix} \dfrac{1.2}{1 + (g_{14}(a_2) + g_{24}(a_2))\eta_2} & -0.1 \\ -0.1 & \dfrac{2(1 + (g_{14}(a_2) + g_{24}(a_2))\eta_2)}{15} \end{bmatrix} \begin{bmatrix} u_{x2} \\ \theta_2 \end{bmatrix} \tag{15}$$

where $H_2 = \left(\frac{1}{3} + g_{11}(a_2)\eta_2 + g_{12}(a_2)\eta_2^2 + (g_{13}(a_2) + g_{23}(a_2))\eta_2^3\right)\left((g_{11}(a_2) + g_{21}(a_2))\eta_2 + 1\right) - \left(\frac{1}{2} + g_{11}(a_2)\eta_2 + \frac{1}{2}(g_{12}(a_2) + g_{22}(a_2))\right)^2$. The expressions of g_{2i} $(i = 1,2,3,4)$ are listed in Appendix A.

The bending deflection of HLS in the Z-axis direction is considered small and can be obtained using Castigliano's second theorem:

$$\Delta_{z2} = \frac{3t_2^2 F_z}{E_2 w_2^3} \int_0^{b_2} \frac{(b_2 - 2y)^2}{\zeta(y)} dy + \frac{12(1+\mu)F_z}{5E_2 w_2} \int_0^{b_2} \frac{1}{\zeta(y)} dy \tag{16}$$

Then the stiffness of an HLS in the Z-axis direction is yielded:

$$K_{z2} = E_2 w_2^3 / \left(3t_2^2 G_1 + 2.4(1+\mu) w_2^2 \lambda_2 b_2\right) \tag{17}$$

where $G_1 = (A_1(a_2, b_2) + A_2(a_2, b_2))/2$, A_2 is shown in Appendix A.

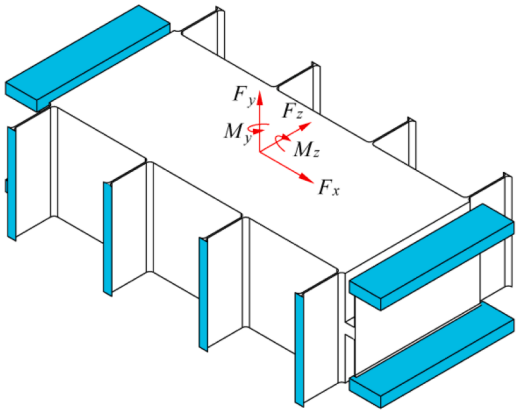

Fig. 5. Guiding mechanism subjected to combined loads.

The torsional stiffness for an HLS around the *Y*-axis can be calculated using the following equation:

$$K_{ay2} = f(\delta_2) \Bigg/ \left(\int_0^{l_2} \frac{7}{2Gw_2 t(x)^3} dx + \int_0^{l_2} \frac{7}{2Gw_2^3 t(x)} dx \right) (\delta_2 = t_2 / w_2) \tag{18}$$

3.3. Kinetostatic model of the guiding mechanism

The planer deflection of CCPMs based on flexure beams was investigated in Ref. [28], while the proposed methods can not capture the coupling of spatial deflections. The use of energy methods can avoid internal loads and considerably reduce the mathematical complexity in the analysis of compliant mechanisms. Hence, the energy method is adopted to obtain the load-deflection relationship of the guiding mechanism. As shown in Fig. 5, the loads applied on the central stage and the corresponding displacement are defined as F_x, F_y, F_z, M_y, M_z, Δ_x, Δ_y, Δ_z, θ_y, θ_z, respectively.

When the central stage is subjected to the combined loads, CFLSs and HLSs are in torsion, tension, and bending along the DOF and DOCs. The deflections of CFLSs are given by:

$$\Delta_{x1} = \Delta_x,\ \Delta_{y1j} = \Delta_y \pm \theta_y R_{1j},\ \Delta_{z1j} = \pm\Delta_z \pm \theta_z R_{1j},\ \theta_{y1} = \theta_y,\ \theta_{z1} = \theta_z \tag{19}$$

where R_{1j} is the distance of CFLS to the torsion axis (for $n = 2i$ or $n = 2i \pm 1$, $j = 1 \ldots i$).

The deflections of HLSs are given by:

$$\Delta_{x2} = \Delta_x,\ \Delta_{y2} = \pm\Delta_y \pm \theta_z R_2,\ \Delta_{z2} = \Delta_z \pm \theta_y R_2, \theta_{y2} = \theta_y,\ \theta_{z2} = \theta_z \tag{20}$$

where R_2 is the distance of HLSs to the torsional axis.

The strain energy of CFLSs is yielded by combining Eqs. (2),(3),(5),(6), and (19):

$$\begin{aligned} V_1 = {} & \frac{K_{z1}}{2} \sum_{j=1}^{i} \left[\left(-\frac{\Delta_z}{l_1} - \frac{\theta_y R_{1j}}{l_1} + s_1 \right)^2 + \left(-\frac{\Delta_z}{l_1} + \frac{\theta_y R_{1j}}{l_1} + s_1 \right)^2 + \left(\frac{\Delta_z}{l_1} - \frac{\theta_y R_{1j}}{l_1} + s_1 \right)^2 + \left(\frac{\Delta_z}{l_1} + \frac{\theta_y R_{1j}}{l_1} + s_1 \right)^2 \right] \\ & + \frac{nEI_1}{l_1} \left(k_{11}^{'0} \left(\frac{\Delta_x}{l_1} \right)^2 + 2k_{12}^{'0} \left(\frac{\Delta_x}{l_1} \right) \theta_y + k_{13}^{'0} \theta_y^2 \right) + nK_{az1} \theta_z^2 + K_{y1} \sum_{j=1}^{i} \left[\left(\frac{\Delta_y}{l_1} - \frac{\theta_z R_{1j}}{l_1} \right)^2 + \left(\frac{\Delta_y}{l_1} + \frac{\theta_z R_{1j}}{l_1} \right)^2 \right] \end{aligned} \tag{21}$$

where $K_{z1} = \frac{k_{14}^{'0} EI_1}{l_1}$ and

$$s_1 = \frac{1}{2} \left[k_{11}^{'1} \left(\frac{\Delta_x}{l_1} \right)^2 + 2k_{12}^{'1} \left(\frac{\Delta_x}{l_1} \right) \theta_y + k_{13}^{'1} \theta_y^2 \right].$$

The strain energy of HLSs is yielded by combining Eqs. (14),(15),(17),(18), and (20):

$$\begin{aligned} V_2 = {} & \frac{K_{y2}}{2} \left[\left(-\frac{\Delta_y}{2} - \frac{\theta_z R_2}{l_2} + s_2 \right)^2 + \left(-\frac{\Delta_y}{2} + \frac{\theta_z R_2}{l_2} + s_2 \right)^2 + \left(\frac{\Delta_y}{2} - \frac{\theta_z R_2}{l_2} + s_2 \right)^2 + \left(\frac{\Delta_y}{2} + \frac{\theta_z R_2}{l_2} + s_2 \right)^2 \right] \\ & + \frac{2EI_2}{l_2} \left(k_{21}^{'0} \left(\frac{\Delta_x}{l_2} \right)^2 + 2k_{22}^{'0} \left(\frac{\Delta_x}{l_2} \right) \theta_z + k_{23}^{'0} \theta_z^2 \right) + \frac{2K_{z2}}{2} \left[\left(\frac{\Delta_z}{l_2} - \frac{\theta_y R_2}{l_2} \right)^2 + \left(\frac{\Delta_z}{l_2} \frac{\theta_y R_2}{l_2} \right)^2 \right] + 2K_{ay2} \theta_y^2 \end{aligned} \tag{22}$$

where $K_{y2}=\frac{k_{24}^{'0}EI_2}{l_2}$ and $s_2=\frac{1}{2}\left[k_{21}^{'1}\left(\frac{\Delta_x}{l_2}\right)^2+2k_{22}^{'1}\left(\frac{\Delta_x}{l_2}\right)\theta_z+k_{23}^{'1}\theta_z^2\right]$.

Thus, the nonlinear strain energy of the guiding mechanism is given as:

$$V_g=V_1+V_2 \tag{23}$$

Then the formulations for loads are obtained by utilizing Castigliano's first theorem. By recognizing that $\theta_y \ll \frac{\Delta_x}{l_1}$ and $\theta_z \ll \frac{\Delta_x}{l_1}$, the load-displacement relationship of the guiding mechanism can be simplified as:

$$F_x=(2nK_{x1}+4K_{x2})\Delta_x+2nK_{ay1}\theta_y+4K_{az2}\theta_2 \tag{24}$$

$$F_y=\left(2nK_{y1}+4K_{y2}\right)\Delta_y \tag{25}$$

$$F_z=(2nK_{z1}+4K_{z2})\Delta_z \tag{26}$$

$$M_y=\left(4K_{z1}\sum_{j=1}^{i}R_{1j}^2+4K_{z2}R_2^2\right)\theta_y+2nK_{ay1}\Delta_x+K_1\theta_y+4K_{ay2}\theta_y \tag{27}$$

$$M_z=\left(4K_{y1}\sum_{j=1}^{i}R_{1j}^2+4K_{y2}R_2^2\right)\theta_z+2nK_{az2}\Delta_x+K_2\theta_z+2nK_{az1}\theta_z \tag{28}$$

where

$$K_{x1}=\frac{EI_1\left(k_{11}^{'0}l_1^2+\frac{1}{2}\left(k_{11}^{'1}\right)^2k_{14}^{'0}\Delta_x^2\right)}{l_1^5},$$

$$K_{x2}=\frac{EI_2\left(k_{21}^{'0}l_2^2+\frac{1}{2}\left(k_{21}^{'1}\right)^2k_{24}^{'0}\Delta_x^2\right)}{l_2^5},$$

$$K_{ay1}=\frac{EI_1\left(\frac{3}{2}k_{11}^{'1}k_{12}^{'1}k_{14}^{'0}\Delta_x^2+k_{12}^{'0}l_1^2\right)}{l_1^4},$$

$$K_{az2}=\frac{EI_2\left(\frac{3}{2}k_{21}^{'1}k_{22}^{'1}k_{24}^{'0}\Delta_x^2+k_{22}^{'0}l_2^2\right)}{l_2^4},$$

$$K_1=\frac{EI_1\left(\frac{1}{2}\left(k_{11}^{'1}k_{13}^{'1}+2\left(k_{12}^{'1}\right)^2\right)k_{14}^{'0}\Delta_x^2+k_{13}^{'0}l_1^2\right)}{l_1^3},$$

$$K_2=\frac{EI_2\left(\frac{1}{2}\left(k_{21}^{'1}k_{23}^{'1}+2\left(k_{22}^{'1}\right)^2\right)k_{24}^{'0}\Delta_x^2+k_{23}^{'0}l_2^2\right)}{l_2^3}.$$

Eqs. (24)–(28) can be expressed as the following matrix:

$$\begin{bmatrix}F_x\\F_y\\F_z\\M_y\\M_z\end{bmatrix}=\begin{bmatrix}K_x&0&0&2nK_{ay1}&4K_{az2}\\0&K_y&0&0&0\\0&0&K_z&0&0\\2nK_{ay1}&0&0&K_{\alpha y}&0\\4K_{az2}&0&0&0&K_{\alpha z}\end{bmatrix}\begin{bmatrix}\Delta_x\\\Delta_y\\\Delta_z\\\theta_y\\\theta_z\end{bmatrix} \tag{29}$$

where $K_x=2nK_{x1}+4K_{x2}$, $K_y=2nK_{y1}+4K_{y2}$, $K_z=2nK_{z1}+4K_{z2}$, $K_{\alpha y}=4K_{z1}\sum_{j=1}^{i}R_{1j}^2+4K_{z2}R_2^2+K_1+4K_{ay2}$, $K_{\alpha z}=4K_{y1}\sum_{j=1}^{i}R_{1j}^2+4K_{y2}R_2^2+K_2+2nK_{az1}$.

As the stiffness matrix in Eq. (29) shows, the displacement along the DOF is coupled with the rotation along the DOC. Enhancing the stiffness along the DOCs is an effective method to reduce the couple displacement. When the stiffness along the DOCs is far large than the driving stiffness, the load-deflection matrix of the guiding mechanism is given as:

$$\begin{bmatrix} F_x \\ F_y \\ F_z \\ M_y \\ M_z \end{bmatrix} = \begin{bmatrix} K_x & 0 & 0 & 0 & 0 \\ 0 & K_y & 0 & 0 & 0 \\ 0 & 0 & K_z & 0 & 0 \\ 0 & 0 & 0 & K_{\alpha y} & 0 \\ 0 & 0 & 0 & 0 & K_{\alpha z} \end{bmatrix} \begin{bmatrix} \Delta_x \\ \Delta_y \\ \Delta_z \\ \theta_y \\ \theta_z \end{bmatrix} \tag{30}$$

Although the matrix is linearized as Eq. (30), the driving stiffness K_x is related to the displacement Δ_x, so it captures the nonlinearity of the guiding mechanism in a large travel range.

3.4. Stress of the guiding mechanism

The stress in the driving direction is crucial for the design of the guiding mechanism. The axial deflections of a fixed-guided CFLS and HLS are $u_{z1} = 0$ and $u_{y2} = 0$.

Substituting $u_{z1} = 0$ and $\theta_1 = 0$ into Eqs. (2) and (3), the driving force and moment at the guided end are yielded:

$$f_1 = \left(\frac{1 + 2g_{11}(a_1)\eta_1}{H_1} + \frac{8.64b_1^2}{(1 + 2g_{14}(a_1)\eta_1)^3}u_{x1}^2\right)u_{x1} \tag{31}$$

$$m_1 = \left(-\frac{1 + 2g_{11}(a_1)\eta_1}{2H_1} - \frac{0.72b_1^2}{(1 + 2g_{14}(a_1)\eta_1)^2}u_{x1}^2\right)u_{x1} \tag{32}$$

Then the moment at the root of the fillet can be obtained:

$$\begin{aligned} M_1 = {} & \frac{u_{x1}E_1I_1}{(1 + 2g_{14}(a_1)\eta_1)^3 l_1}\left(-\frac{1 + 2g_{11}(a_1)\eta_1}{2H_1}(1 + 2g_{14}(a_1)\eta_2)^3 - 7.92(1 + 2g_{14}(a_1)\eta_2)b_1^2u_{x1}^2\right. \\ & \left. + \left(\frac{2g_{11}(a_1)\eta_1 + 1}{H_1}(1 + 2g_{14}(a_1)\eta_2)^3 + 8.64b_1^2u_{x1}^2\right)(1 - a_1 / b_1)\right) \end{aligned} \tag{33}$$

Considering the influence of the stress concentration factor ($k_b = (a + 0.253)/(a + 0.097)$ for bending and $k_t = (a + 0.371)/(a + 0.097)$ for tension, as provided in Ref. [31]), the maximum bending stress and maximum tensile stress can be expressed as:

$$\begin{aligned} \sigma_{b1} = {} & \frac{u_{x1}E_1k_{b1}}{2(1 + 2g_{14}(a_1)\eta_1)^3 b_1}\left(-\frac{1 + 2g_{11}(a_1)\eta_1}{2H_1}(1 + 2g_{14}(a_1)\eta_2)^3 - 7.92(1 + 2g_{14}(a_1)\eta_2)b_1^2u_{x1}^2\right. \\ & \left. + \left(\frac{2g_{11}(a_1)\eta_1 + 1}{H_1}(1 + 2g_{14}(a_1)\eta_2)^3 + 8.64b_1^2u_{x1}^2\right)\left(1 - \frac{a_1}{b_1}\right)\right) \end{aligned} \tag{34}$$

$$\sigma_{t1} = \frac{0.6u_{x1}^2E_1k_{t1}}{(1 + 2g_{14}(a_1)\eta_2)^2} \tag{35}$$

The total maximum stress of CFLS can be obtained by the following equation:

$$\sigma_{\max 1} = \sigma_{t1} + \sigma_{b1} \tag{36}$$

The stress of HLSs can be obtained in the same way as CFLSs, which can be calculated using the following equations:

$$\sigma_{b2} = \frac{u_{x2}E_2k_{b2}}{2\lambda_2^3 b_2}\left(\begin{array}{l} -\dfrac{1 + 2g_{11}(a_2)\eta_2 + (g_{12}(a_2) + g_{22}(a_2))}{2H_2}\lambda_2^3 - 7.92\lambda_2 b_2^2u_{x2}^2 + \\ \left(\dfrac{1 + (g_{11}(a_2) + g_{21}(a_2))\eta_2}{H_2}\lambda_2^3 + 8.64b_2^2u_{x2}^2\right)\left(1 - \dfrac{a_2}{b_2}\right) \end{array}\right) \tag{37}$$

$$\sigma_{t2} = \frac{0.6u_{x2}^2E_2k_{t2}}{(1 + (g_{14}(a_2) + g_{24}(a_2))\eta_2)^2} \tag{38}$$

$$\sigma_{\max 2} = \sigma_{t2} + \sigma_{b2} \tag{39}$$

where $\lambda_2 = 1 + (g_{14}(a_2) + g_{24}(a_2))\eta_2$.

3.5. Frequency of the guiding mechanism

The equivalent mass of the guiding mechanism can be calculated as:

$$M_e = M_0 + \left(2ncl_1t_1 + 4n\left(1 - \frac{\pi}{4}\right)r_1^2\right)\rho_1w_1 + \left(2mcl_2t_2 + 2m\left(1 - \frac{\pi}{4}\right)r_2^2\right)\rho_2w_2 \tag{40}$$

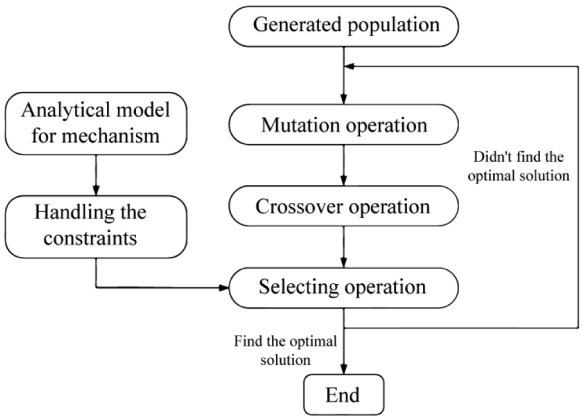

Fig. 6. Optimization processing.

Table 1
. Parameters of the guiding mechanism.

n	r_1(mm)	t_1(mm)	w_1(mm)	r_2(mm)	l_2(mm)
2	1.36	0.76	42.81	0.60	13.90
3	1.23	0.67	44.39	0.56	14.69
4	1.13	0.61	45.55	0.55	15.27
5	1.07	0.57	46.46	0.55	15.73
6	1.01	0.53	47.20	0.54	16.10
7	0.97	0.51	47.83	0.54	16.41
8	0.94	0.48	48.37	0.54	16.68

Table 2
Main physical properties of the guiding mechanism.

n	σ_{max} (MPa)	f_r (Hz)	K_x $\left(\frac{N}{\mu m}\right)$	K_y $\left(\frac{N}{\mu m}\right)$	K_z $\left(\frac{N}{\mu m}\right)$	$K_{\alpha y}$ $\left(\frac{N\cdot m}{\mu rad}\right)$	$K_{\alpha z}$ $\left(\frac{N\cdot m}{\mu rad}\right)$	M_t (g)
2	277	201	1.00	463	590	2.86	2.47	633.5
3	248	197	1.00	498	760	2.66	2.32	660.0
4	229	195	1.00	534	917	2.74	2.29	679.6
5	216	193	1.00	570	1065	2.89	2.29	695.4
6	206	191	1.00	607	1205	3.07	2.31	708.5
7	198	190	1.00	642	1339	3.25	2.34	719.8
8	192	188	1.00	677	1467	3.44	2.37	729.8

where M_0 is the mass of the central stage, c is the equivalent mass factor of leaf spring which is determined as 13/35 according to Ref. [36]. ρ_1 and ρ_2 are the mass destiny of material of CFLSs and HLSs, respectively.

Then the total mass of the guiding mechanism can be expressed as:

$$M_t = M_0 + \left(2nl_1t_1 + 8n\left(1-\frac{\pi}{4}\right)r_1^2\right)\rho_1 w_1 + \left(2ml_2t_2 + 6m\left(1-\frac{\pi}{4}\right)r_2^2\right)\rho_2 w_2 \tag{41}$$

The resonant frequency of the guiding mechanism is derived as:

$$f_r = \frac{1}{2\pi}\sqrt{\frac{K_x}{M_e}} \tag{42}$$

4. Optimization design

4.1. Optimization model

The stiffness along the DOC should be large enough to avoid displacement coupling. Maximum stress has a crucial influence on the fatigue life of mechanisms in some high-speed and high-acceleration applications. Therefore, the design objective is to minimize the total mass and maximum stress of the guiding mechanism by determining the optimal parameters of CFLSs and HLSs which satisfy the

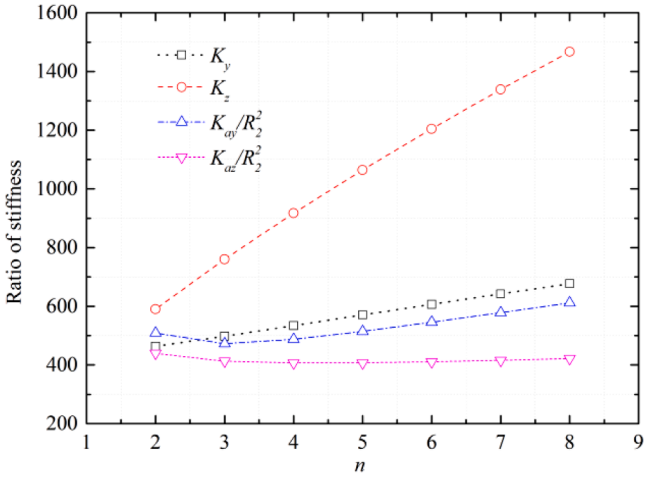

Fig. 7. The ratio of stiffness along the DOC to it along the DOF.

Table 3
Verification of the optimal design.

	Design values	FEA results	Error %
f_r	195 Hz	202 Hz	3.4
K_x	1.00 N/μm	1.07 N/μm	7.3
K_y	534 N/μm	476 N/μm	12
K_z	917 N/μm	877 N/μm	4.5
$K_{\alpha y}$	2.74 N · m/μrad	2.73 N · m/μrad	0.3
$K_{\alpha z}$	2.29 N · m/μrad	2.09 N · m/μrad	9.3
$\sigma_{\max}$	229 MPa	233 MPa	1.7

frequency and stiffness constraints. The optimization objective can be expressed as:

$$\begin{aligned} &\text{Find } (n, r_1, t_1, w_1, r_2, l_2) \\ &\text{to minimize}: F_c = M_t + c_1 \max(\sigma_{\max 1}, \sigma_{\max 2})/\sigma_{\max 0} \\ &\text{subject to}: f_r > f_{r0} \\ &K_x = K_{x0} \\ &K_y > K_{y0} \\ &K_z > K_{z0} \\ &K_{\alpha y} > K_{\alpha y0} \\ &K_{\alpha z} > K_{\alpha z0} \end{aligned} \tag{43}$$

where c_1 is the weight coefficients.

The design model presented in Eq. (43) contains the topology structure (the group numbers of CFLSs and their location) and size parameters (parameters of CFLS and HLS). The nonlinear constraints are handled with the self-adaptive penalty function [37]. Then optimal parameters are obtained using the differential evolution algorithm [38–40].

As shown in Fig. 6, the analytical model for the mechanism is built at the first stage and then the constraints are handled with a self-adaptive penalty function and the differential evolution algorithm is utilized to obtain the optimal parameters of the flexure hinge which is consists of mutation operation, interlace operation, and selecting operation. The determining of optimal group number and the corresponding optimal parameters can be outlined as follows:

Step 1: Let $n_0 = n = 2$.

Step 2: Obtained the optimal parameters by utilizing the optimization processing shown in Fig. 6.

Step 3: If $K_y < K_{y0}$, $n = n + 1$ and return to step 2.

Step 4: If $K_y > K_{y0}$, output n and the parameters of CFLS and HLS, and calculate the properties of the mechanism.

4.2. Design case

Aluminum alloy is selected as the material, whose Young's modulus is $E = 71.7$ GPa, Poisson's ratio is $\mu = 0.33$, and mass density is $\rho = 2700$ Kg/m^3. The length and width of the design area are 150 and 100 mm. The length of CFLSs is $l_1 = 20$ mm. The thickness of HLSs is $t_2 = 0.25$ mm. The static stiffness in the driving direction is $K_x = 1$ N/μm. The payload stiffness in the Z-axis direction K_z and it

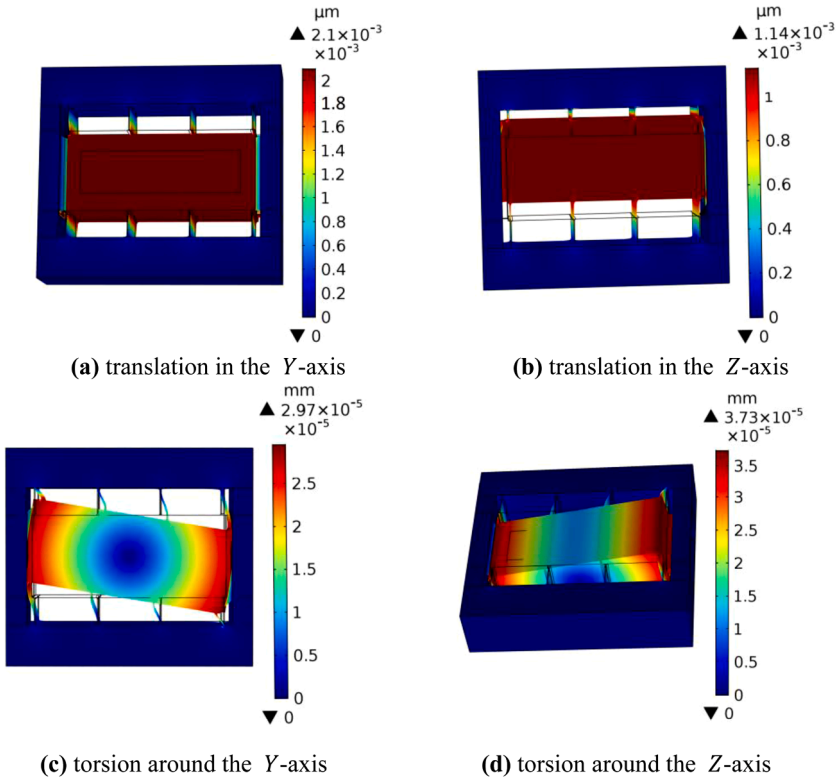

Fig. 8. Deflections in the DOC directions.

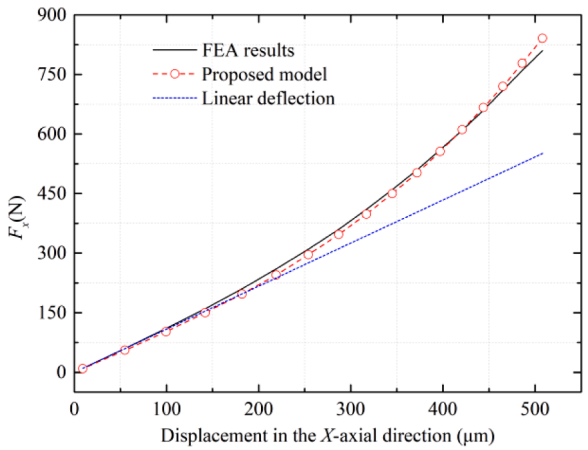

Fig. 9. Load-displacement relationship of the guiding mechanism.

in the and Y-axis direction K_y are large than 500 N/μm. The torsional stiffness around Z-axis K_{az} and it around Y-axis K_{zy} are large than 1 N · m/μrad. The resonant frequency f_r is large than 150 Hz. The maximum stress is less than $\sigma_{max0} = 250$ MPa when the travel range of the guiding mechanism reaches 500 μm.

The optimal parameters n, r_1, t_1, w_1, r_2 and l_2 are listed in Table 1. The corresponding physical properties presented in Table 2 show that the maximum stress is 229 MPa when the group number n is large than 4 which satisfies the desired value of 250 MPa and the stiffness $K_y = 534$ N/μm matches the desired value of 500 N/μm. The stiffness along the DOC increases and the maximum stress decreases with the increase of group number which is beneficial for the applications; however, and mass of the guiding mechanism increases with the group number, and the frequency decreases. Therefore, the optimal parameters are determined as n= 4, $r_1 = 1.13$ mm, $t_1 =$ 0.61 mm, $w_1 =$ 45.55 mm, $r_2 = 0.55$ mm, $l_2 =$ 15.27 mm.

The ratios of stiffness along the DOC and DOF are plotted in Fig. 7, which shows that the stiffness along the DOC is far large than it

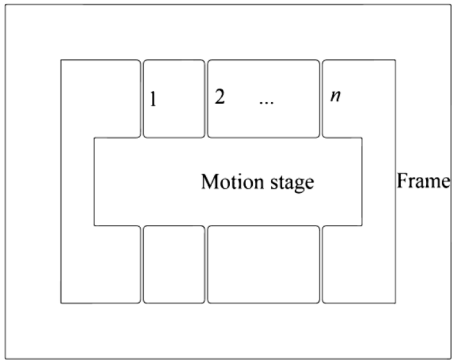

Fig. 10. Schematic diagram of the traditional guiding mechanism.

Table 4
Parameters of the mentioned guiding mechanism.

n	r(mm)	t(mm)	w(mm)	σ_{max}(MPa)	fre(Hz)	K_x(N/μm)	M_t(g)
2	1.41	0.80	42.75	287	201	1.00	631.4
3	1.26	0.69	44.37	255	197	1.00	657.9
4	1.16	0.63	45.54	234	195	1.00	677.5
5	1.09	0.58	46.45	220	193	1.00	693.1
6	1.03	0.55	47.2	210	191	1.00	706.3
7	0.99	0.52	47.82	201	190	1.00	717.5
8	0.95	0.49	48.37	195	188	1.00	727.5

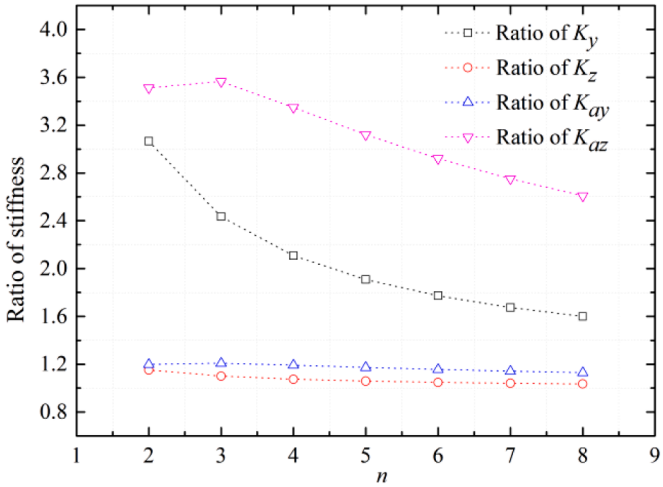

Fig. 11. The ratio of stiffness along the DOC for two types of designs.

along the DOF (large than 400 times) and the group number of CFLSs provides a major improvement in the stiffness along the Z-axis direction and minor stiffness improvement along other DOC directions.

5. Verification with FEA

An FEA model is built in COMSOL Multiphysics 5.3 by utilizing the optimal parameters determined in Section 4.2 and FEA results are obtained and listed in Table 3.

The deflections along the DOC of a guiding mechanism subjected to a unit force or moment are depicted in Fig. 8. The maximum deflection of the mechanism along the Y-axis and Z-axis are 0.00213 μm and 0.00114 μm when the mechanism is subjected to a unit load along Y-axis and Z-axis, respectively. The maximum deflection of mechanism around the Y-axis and Z-axis are 0.0297 μm and 0.0373 μm when the mechanism is subjected to a unit moment around the Y-axis and Z-axis, respectively.

The nonlinear displacement in the X-axis direction is plotted in Fig. 9. The comparison illustrates that the proposed model is in good

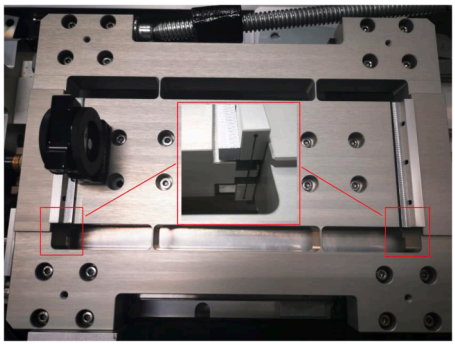

Fig. 12. Guiding mechanism installing leaf springs.

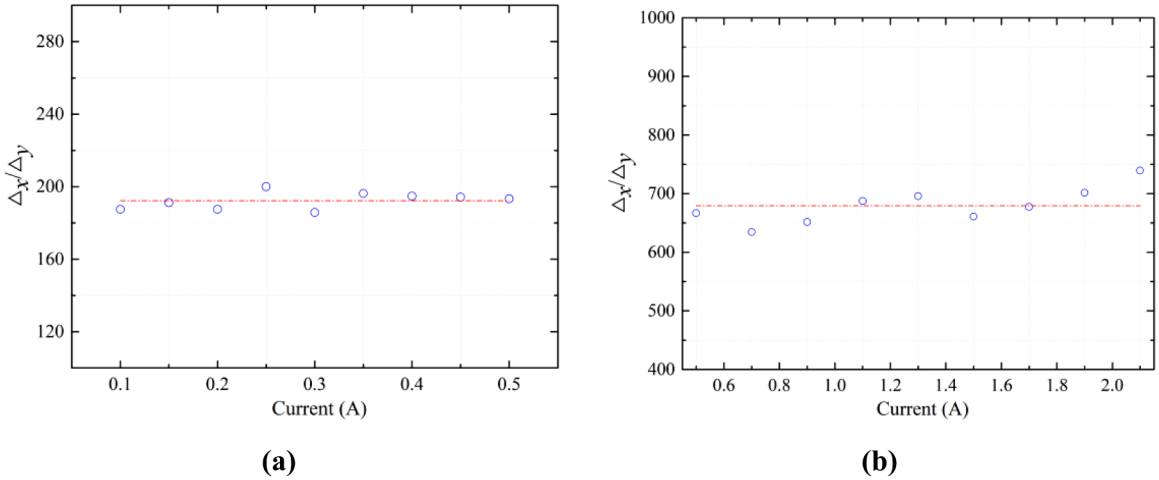

Fig. 13. Test results for two types of designs (a) displacement ratios for the traditional mechanism, (b) displacement ratios for the proposed mechanism.

agreement with the FEA results. As Fig. 9 shown, the stiffness along the DOF is increased by 48% for the maximum stroke, which leads to a decrease in the ratio of stiffness along the DOC to it along the DOF.

6. Comparison with guiding mechanism without HLSs

Ref. [33] employed CFLSs for a guiding mechanism to improve the maximum stress of beam-based design, showing that the maximum stress of leaf spring is reduced by 33% for the same travel range. The mentioned mechanism, whose schematic diagram is shown in Fig. 10, is optimized to minimize the total mass and maximum stress by determining the optimal parameters r and t with the same constraints as shown in Eq. (43). The optimal results for different group number n are listed in Table 4, which indicate that the frequency, total mass, and maximum stress of the two types of designs are close.

The corresponding stiffness ratios of two types of designs in the DOC directions are plotted in Fig. 11 which illustrates that the new design provides a considerable improvement in the stiffness K_y and K_{az} and a slight improvement in the stiffness K_y and K_{ay}.

7. Experimental results

The guiding mechanism is manufactured for experimental investigations, in which the HLSs are displaced by the thin leaf springs produced by spring steel 65 Mn (the thickness is 0.2 mm) for its high fatigue strength, as shown in Fig. 12. When the leaf springs are disassembled, the proposed design becomes the mentioned guide mechanism shown in Fig. 10. The efficiency of the proposed design is illustrated by measuring the stiffness ratio of the guiding mechanism in two different states (leaf springs are assembled or not).

Tests are carried out to illustrate the efficiency of the proposed structure in the improvement of torsional stiffness around the Z-axis. The mechanism for the macro-micro compounded system is fixed on the rigid guide and driven by Ironless Motor (AUM3-S3, from Akribis Systems Inc.). The displacement of the guiding mechanism in the X-axis direction is measured using Incremental Encoder System (RGH22, from Renishaw Inc.) with Linear Scale (RGS20, from Renishaw Inc.), and the displacement in the Y-axis direction caused by the torsional moment is obtained by using Laser System (XL-80 from Renishaw Inc.).

The torsional stiffness of the traditional mechanism and the proposed mechanism are measured as 3.68 N · m/μrad and 23.83 N · m /μrad, respectively. The displacement ratios for two types of mechanisms are plotted in Fig. 13(a) and (b). The average ratio of the displacement of the traditional guiding mechanism along the DOF to that along the DOC is 192 for different driving forces, while the proposed mechanism increases this value to 679. The increase rate reaches 254%.

8. Conclusions

A new guiding mechanism employing orthogonally oriented CFLSs and HLSs is proposed in this paper to provide a high stiffness ratio along the DOC to it along the DOF and reduce the stress concentration. The nonlinear deflection and maximum stress of the guiding mechanism are investigated for large-stroke applications. The kinetostatic model is obtained by utilizing the energy method for the simultaneous optimal design of topology and size. An optimization design is carried out to minimize the total mass and maximum stress of guiding mechanism subjecting to the stiffness and frequency constraints. The optimization results are verified by FEA results. Comparison with normal design indicates that the proposed guiding mechanism enhances the stiffness along the DOC effectively, which has been verified by experimental results.

Declaration of Competing Interest

We declare that we have no financial and personal relationships with other people or organizations that can inappropriately influence our work, there is no professional or other personal interest of any nature or kind in any product, service and/or company that could be construed as influencing the position presented in, or the review of, the manuscript entitled, “A compliant guiding mechanism utilizing orthogonally oriented flexures with enhanced stiffness in degrees-of-constraint”.

Acknowledgments

This work was supported in part by the National Natural Science Foundation of China (Grant Nos. 51875108, 51905107, 51975128, and 61973093).

Appendix A

The expressions of g_{1i} and g_{2i} ($i = 1,2,3,4$) are listed as:

$$g_{11}(a) = \frac{6a(2a+1)}{(4a+1)^{2.5}}\arctan\left(\sqrt{4a+1}\right) + \frac{6a^2+4a+1}{(2a+1)(4a+1)^2} - 1 \tag{A.1}$$

$$g_{12}(a) = \frac{-12a(2a+1)}{(4a+1)^{2.5}}\arctan\left(\sqrt{4a+1}\right) + \frac{2a-1}{(4a+1)^2} + 1 \tag{A.2}$$

$$g_{13}(a) = \frac{(6a^2-4a-1)(2a+1)^3}{4a^3(4a+1)^{2.5}}\arctan\left(\sqrt{4a+1}\right) - \frac{20a^3-6a^2-6a-1}{4a^2(4a+1)^2} + \frac{\pi}{16a^3} - \frac{1}{3} \tag{A.3}$$

$$g_{14}(a) = \frac{2a+1}{a\sqrt{4a+1}}\arctan\sqrt{4a+1} - \frac{\pi}{4a} - 1 \tag{A.4}$$

$$g_{21}(a) = \frac{3a(a+1)}{(2a+1)^{2.5}}\arctan\left(\sqrt{2a+1}\right) + \frac{3a^2+4a+2}{2(2a+1)(4a+1)^2} - 1 \tag{A.5}$$

$$g_{22}(a) = \frac{6a(a+1)}{(2a+1)^{2.5}}\arctan\left(\sqrt{2a+1}\right) - \frac{a-1}{(4a+1)^2} - 1 \tag{A.6}$$

$$g_{23}(a) = \frac{(3a^2-4a-2)(a+1)^3}{a^3(2a+1)^{2.5}}\arctan\left(\sqrt{2a+1}\right) - \frac{5a^3-3a^2-6a-2}{2a^2(4a+1)^2} + \frac{\pi}{2a^3} - \frac{1}{3} \tag{A.7}$$

$$g_{24}(a) = \frac{2(a+1)}{a\sqrt{2a+1}}\arctan\sqrt{2a+1} - \frac{\pi}{2a} - 1 \tag{A.8}$$

The expressions of A_1 and A_2 are listed as:

$$\begin{aligned} A_1(a,b) = {} & \frac{2(2a+1)\left((b-2a)^2-4a-1\right)\arctan\sqrt{4a+1}}{\sqrt{4a+1}} + \frac{(b-2a)^3}{3} + 2a(6a+1-2b) + 2(2a+1)(b-2a)\ln(2a+1) \\ & + \pi\left(-a^2+2ab-\frac{b^2}{2}+2a+\frac{1}{2}\right) \end{aligned} \tag{A.9}$$

$$A_2(a,b) = 4(a+1)\left((b-2a)^2 - 4(2a+1)\right)\frac{\arctan\sqrt{2a+1}}{\sqrt{2a+1}} + 8(a+1)(b-2a)\ln(a+1) + \left(-2a^2+4ab-b^2+8a+4\right)\pi + \frac{(b-2a)^3}{3} + 24a^2 - 8ab + 8a \tag{A.10}$$

References

[1] S. Kang, M.G. Lee, Y.M. Choi, Six degrees-of-freedom direct-driven nanopositioning stage using crab-leg flexures, IEEE/ASME Trans. Mechatron. 25 (2020) 513–525.
[2] H. Kim, J. Kim, D. Ahn, D. Gweon, Development of a nanoprecision 3-DOF vertical positioning system with a flexure hinge, IEEE Trans. Nanotechnol. 12 (2013) 234–245.
[3] J.J. Kim, Y.M. Choi, D. Ahn, B. Hwang, D.G. Gweon, J. Jeong, A millimeter-range flexure-based nano-positioning stage using a self-guided displacement amplification mechanism, Mech. Mach. Theory 50 (2012) 109–120.
[4] N. Lobontiu, Compliance-based modeling and design of straight-axis/circular-axis flexible hinges with small out-of-plane deformations, Mech. Mach. Theory 80 (2014) 166–183.
[5] S. Wan, Q. Xu, Design and analysis of a new compliant XY micropositioning stage based on Roberts mechanism, Mech. Mach. Theory 95 (2016) 125–139.
[6] Q. Xu, Design and development of a flexure-based dual-stage nanopositioning system with minimum interference behavior, IEEE Trans. Autom. Sci. Eng. 9 (2012) 554–563.
[7] X. Zhang, Q. Xu, Design and testing of a new 3-DOF spatial flexure parallel micropositioning stage, Int. J. Precis. Eng. Manuf. 19 (2018) 109–118.
[8] W. Johnson, C. Dai, J. Liu, X. Wang, D.K. Luu, Z. Zhang, C. Ru, C. Zhou, M. Tan, H. Pu, S. Xie, Y. Peng, J. Luo, Y. Sun, A flexure-guided piezo drill for penetrating the zona pellucida of mammalian oocytes, IEEE Trans. Biomed. Eng. 65 (2018) 678–686.
[9] Y.Z. Wei, Q.S. Xu, Design of a PVDF-MFC force sensor for robot-assisted single cell microinjection, IEEE Sens. J. 17 (2017) 3975–3982.
[10] Y.Z. Wei, Q.S. Xu, Design and testing of a new force-sensing cell microinjector based on soft flexure mechanism, IEEE Sens. J. 19 (2019) 6012–6019.
[11] S. Yang, Q. Xu, Z. Nan, Design and development of a dual-axis force sensing mems microgripper, J. Mech. Rob. 9 (6) (2017), 061011.
[12] K.Y. Huang, C.J. Lee, Design and development of a piezoelectric actuator for the scanning probe microscope used in ultrahigh vacuum, J. Mech. 23 (2007) 117–126.
[13] D. Kang, K. Kim, D. Kim, J. Shim, D.G. Gweon, J. Jeong, Optimal design of high precision XY-scanner with nanometer-level resolution and millimeter-level working range, Mechatronics 19 (2009) 562–570.
[14] Y.K. Yong, B. Bhikkaji, S.O.R. Moheimani, Design, Modeling, and FPAA-based control of a high-speed atomic force microscope nanopositioner, IEEE/ASME Trans. Mechatron. 18 (2013) 1060–1071.
[15] P. Liu, P. Yan, A new model analysis approach for bridge-type amplifiers supporting nano-stage design, Mech. Mach. Theory 99 (2016) 176–188.
[16] H. Tang, J. Gao, X. Chen, K.M. Yu, S. To, Y. He, X. Chen, Z. Zheng, S. He, C. Chen, Y. Li, Development and repetitive-compensated PID control of a nanopositioning stage with large-stroke and decoupling property, IEEE Trans. Ind. Electron. 65 (2018) 3995–4005.
[17] M. Ling, J. Cao, Z. Jiang, J. Lin, Modular kinematics and statics modeling for precision positioning stage, Mech. Mach. Theory 107 (2017) 274–282.
[18] R. Lin, Y.Z. Li, Y.X. Zhang, T. Wang, Z. Wang, Z. Song, Z. Dou, J. Qian, Design of a flexure-based mixed-kinematic XY high-precision positioning platform with large range, Mech. Mach. Theory 142 (2019), 103609.
[19] X. Zhang, Q. Xu, Design and development of a new 3-DOF active-type constant-force compliant parallel stage, Mech. Mach. Theory 140 (2019) 654–665.
[20] M.X. Ling, J.Y. Cao, Q.S. Li, J. Zhuang, Design, pseudostatic model, and PVDF-based motion sensing of a piezo-actuated XYZ flexure manipulator, IEEE/ASME Trans. Mechatron. 23 (2018) 2837–2848.
[21] P.B. Liu, P. Yan, Z. Zhang, T.T. Leng, Flexure-hinges guided nano-stage for precision manipulations: design, modeling and control, Int. J. Precis. Eng. Manuf. 16 (2015) 2245–2254.
[22] D. Ahn, Y.M. Choi, J. Jeong, Design of a four-degree-of-freedom nano positioner utilizing electromagnetic actuators and flexure mechanisms, Rev. Sci. Instrum. 86 (3) (2015), 035101.
[23] X.B. Zhu, X. Xu, Z.J. Wen, J.Q. Ren, P.K. Liu, A novel flexure-based vertical nanopositioning stage with large travel range, Rev. Sci. Instrum. 86 (2015), 105112.
[24] H. Malaeke, H. Moeenfard, A novel flexure beam module with low stiffness loss in compliant mechanisms, Precis Eng. 48 (2017) 216–233.
[25] H. Zhao, D. Han, L. Zhang, S. Bi, Design of a stiffness-adjustable compliant linear-motion mechanism, Precis. Eng. 48 (2017) 305–314.
[26] G. Hao, H. Li, Extended Static Modeling and analysis of compliant compound parallelogram mechanisms considering the initial internal axial force, J. Mech. Rob. 8 (4) (2016), 041008.
[27] G.B. Hao, J.J. Yu, Design, modeling and analysis of a completely-decoupled XY compliant parallel manipulator, Mech. Mach. Theory 102 (2016) 179–195.
[28] G. Hao, H. Li, Nonlinear analytical modeling and characteristic analysis of a class of compound multibeam parallelogram mechanisms, J. Mech. Rob. 7 (4) (2015), 041016.
[29] G. Hao, X. Kong, A novel large-range XY compliant parallel manipulator with enhanced out-of-plane stiffness, J. Mech. Des. 134 (6) (2012), 061009.
[30] Y. Bai, X. Chen, Z. Yang, Design of rigid motion and elastic deformation parallel driven based macro-micro compounded positioning stage, Sci. Chin. Technol. Sci. 49 (2019) 669–680, in Chinese.
[31] G. Chen, J. Wang, X. Liu, Generalized equations for estimating stress concentration factors of various notch flexure hinges, J. Mech. Des. 136 (3) (2014), 031009.
[32] J.F. Gomez, J.D. Booker, P.H. Mellor, 2D shape optimization of leaf-type crossed flexure pivot springs for minimum stress, Precis. Eng. 42 (2015) 6–21.
[33] R.Q. Li, Z.J. Yang, G.M. Chen, B.S. Wu, Analytical solutions for nonlinear deflections of corner-fillet leaf-springs, Mech. Mach. Theory 157 (2021), 104182.
[34] M. Radgolchin, H. Moeenfard, A constraint model for beam flexure modules with an intermediate semi-rigid element, Int. J. Mech. Sci. 122 (2017) 167–183.
[35] G.M. Chen, L.L. Howell, Two general solutions of torsional compliance for variable rectangular cross-section hinges in compliant mechanisms, Precis. Eng. 33 (2009) 268–274.
[36] Z. Yang, Y. Bai, X. Chen, Simultaneous optimal design of topology and size for a flexure-hinge-based guiding mechanism to minimize mass under stiffness and frequency constraints, Eng. Optim. 49 (2017) 948–961.
[37] B. Tessema, G.G. Yen, A self adaptive penalty function based algorithm for constrained optimization, in: Proceedings of the IEEE Congress on Evolutionary Computation, Vancouver, CANADA 1-6, 2006. Vols246-+.
[38] J. Liu, J. Lampinen, A fuzzy adaptive differential evolution algorithm, Soft Comput. 9 (2005) 448–462.
[39] R. Mallipeddi, P.N. Suganthan, Q.K. Pan, M.F. Tasgetiren, Differential evolution algorithm with ensemble of parameters and mutation strategies, Appl. Soft Comput. 11 (2011) 1679–1696.
[40] A.K. Qin, V.L. Huang, P.N. Suganthan, Differential evolution algorithm with strategy adaptation for global numerical optimization, IEEE Trans. Evol. Comput. 13 (2009) 398–417.